International Journal of Remote Sensing
Vol. 32, No. 12, 20 June 2011, 3345–3371

Taylor & Francis
Taylor & Francis Group

Detecting ground fog from space – a microphysics-based approach

JAN CERMAK*† and JÖRG BENDIX‡
†Institute for Atmospheric and Climate Science, ETH Zurich, Zurich, Switzerland (formerly at ‡)
‡Laboratory for Climatology and Remote Sensing (LCRS), Faculty of Geography, Philipps-Universität Marburg, Marburg, Germany

(*Received 15 April 2009; in final form 19 February 2010*)

The detection of ground fog from satellite data is of interest in operational now-casting applications, as well as in studies of the climate system. A discrimination between fog at the ground and other low-stratus situations from satellite data requires information on cloud vertical geometry to establish whether the cloud touches the ground. This article introduces a technique that allows for the discrimination between low stratus and (ground) fog on the basis of geostationary satellite imagery. The cloud-base height is derived using a subadiabatic model of cloud microphysics. In this model, the cloud base is varied until model liquid–water path matches that retrieved from satellite data. The performance of this technique is shown to be good in a comparison with METeorological Aerodrome Report data comprising 1030 satellite scenes. With a hit rate of 81% and a threat score of 0.62, the skill is satisfactory.

1. Introduction

1.1 *Motivation*

Many applications in operational weather forecasting and climatological analyses require information on ground-fog occurrence in time and space (for an overview, see Jacobs *et al.* 2008). The field of satellite-based fog and low-stratus detection has seen steady progress with the development of new satellite sensors (see Gultepe *et al.* 2007, for an overview). Low-stratus detection at night was first implemented by Eyre *et al.* (1984) on the Advanced Very High Resolution Radiometer (AVHRR). This technique has later been ported to various other sensors (e.g. Greenwald and Christopher 2000). Dedicated daytime techniques were recently presented by Bendix *et al.* (2006) and Cermak and Bendix (2008).

However, none of these approaches differentiates between fog at the ground and other low-stratus clouds. Still, the term 'fog' is used widely and liberally in satellite-based low-stratus detection papers. In this study, 'fog' is used only to refer to actual fog at the ground ('ground fog'). From the satellite perspective, fog can be seen as a cloud touching the ground in a given location (see figure 1), or

$$z_b \leq z_s \rightarrow \text{fog}, \tag{1}$$

*Corresponding author. Email: jan.cermak@env.ethz.ch

International Journal of Remote Sensing
ISSN 0143-1161 print/ISSN 1366-5901 online © 2011 Taylor & Francis
http://www.tandf.co.uk/journals
DOI: 10.1080/01431161003747505

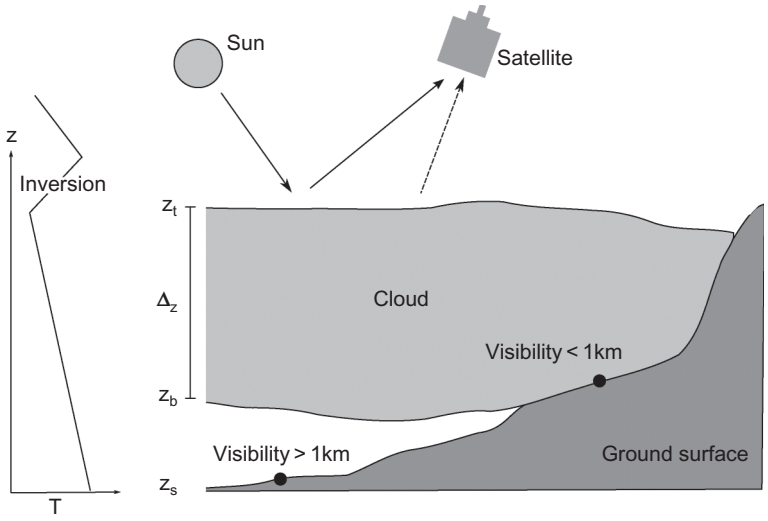

Figure 1. Ground-fog detection requires knowledge of cloud geometry, that is, three-dimensional information on the cloud, including its boundaries (z_t and z_b) and thickness (Δ_z), as well as surface elevation z_s. These properties manifest themselves in the shortwave and longwave radiation transferred from the cloud to the satellite sensor.

where z_b is the cloud-base height and z_s is the surface elevation. While the latter can be extracted from a digital elevation model (DEM), the former needs to be derived from satellite data. Cloud-base height can be computed as

$$z_b = z_t - \Delta_z, \tag{2}$$

where z_t is the cloud-top height and Δ_z is the cloud geometrical thickness. Accordingly, these two parameters need to be determined in order to discriminate between fog and other low stratus. The determination of z_t has been discussed in depth in Cermak (2006): cloud-top height is derived in a twofold procedure involving the analysis of the terrain around a low-stratus-covered area and an assumed atmospheric lapse rate. The more challenging part is the determination of cloud geometrical thickness. Accordingly, the focus of this study will be on the development of a method to determine low-stratus thickness from satellite data.

Section 2 describes previous approaches to thickness retrieval, section 3 presents method development, section 4 includes a numerical validation study and section 5 identifies areas for further research.

1.2 *Data and domain*

Operational applications, in particular, require information at a high temporal resolution. Therefore, geostationary satellite data are more suited for fog detection than data from polar orbiters. In this study, Meteosat Second Generation (MSG) Spinning-Enhanced Visible and Infrared Imager (SEVIRI) data are used. This study focuses on Europe (the full domain is shown in figure 12); a variety of fog situations are found here, and the availability of data for algorithm development and validation are good. An overview of the products and channels used in this study is given in table 1. Detailed explanations follow below.

Table 1. SEVIRI products and channels used in the study.

Product	Channels	Purpose	Reference
Low-stratus product	0.6, 0.8, 1.6, 3.9, 8.7, 10.8, 12.0 μm	Potential fog area	Cermak and Bendix (2008)
Cloud optical thickness	0.6, 3.9 μm	Liquid–water path	Kawamoto *et al.* (2001)
Cloud-droplet effective radius	0.6, 3.9 μm	Liquid–water path	Kawamoto *et al.* (2001)

2. Previous approaches to satellite-based cloud-geometry retrieval

Existing cloud-thickness retrieval techniques can be classified into three main strands: simple parameterizations, approximations assuming an adiabatic distribution of cloud liquid water and pseudosounding methods that try to obtain information on the actual vertical distribution of cloud properties. The potentials and limitations of each group are explored in the following.

2.1 *Simple parameterizations*

The simplest kind of approach to cloud-thickness computation relies on parameterizations of one or more parameters related to thickness. These methods usually yield only very rough approximations.

Ellrod (2002) applies a threshold to the difference of Geostationary Operational Environmental Satellite (GOES) infrared brightness temperatures between clear and cloudy pixels to identify cloud-base heights $<$1000 ft ($\sim$300 m). This approach relies on the assumptions that a) a low-temperature difference indicates low cloud-top height, and b) all clouds identified are of sufficient thickness for their bases to reach 1000 ft. While the first of these assumptions will be roughly accurate in most situations, the second condition is not solid enough for application in the context of the present study.

A range of schemes implicitly or explicitly relate cloud optical bulk parameters to cloud geometrical thickness. The brightness–temperature difference between 10.8 and 3.9 μm can be linked to cloud optical depth (cf. Hunt 1973). Based on this relationship, and assuming a constant vertical stratification, the brightness–temperature difference is used by Ellrod (1995) to estimate fog geometrical thickness from GOES imagery. This method provides only very rough approximations to cloud thickness, as it only considers optical depth (by proxy).

Some authors present estimates of the average liquid–water content $\overline{\rho_c}$ of a cloud. Dividing satellite-retrieved cloud liquid–water path W by $\overline{\rho_c}$ yields an estimate of cloud thickness. Stephens (1979), Hess *et al.* (1998) and Korolev *et al.* (2001) present such liquid–water content values for a range of different cloud types (0.05 to 0.30 g m^{-3} for stratus); Nakajima and Nakajima (1995) use a fixed value of 0.154 g m^{-3} for stratus and Hutchison (2002) uses values of 0.20 to 0.45 g m^{-3}. The obvious problem of this type of method is the wide range of possible values of $\overline{\rho_c}$ (variation by a factor of 9 in the estimates presented above).

Other authors relate $\overline{\rho_c}$ to temperature (Gultepe and Isaac 1997, Liou 2002) and droplet effective radius (Martin *et al.* 1994, McFarlane *et al.* 1995). Although these approximations may be useful for local application, vertical variation within a cloud

is only insufficiently represented so that $\overline{\rho_c}$ found in this way is no sound basis for cloud-thickness determination.

2.2 *Adiabatic approximations*

Several authors try to compensate the lack of vertical cloud information by assuming an adiabatic cloud profile. In these situations, liquid–water content is expected to increase monotonically with height over cloud base. The adiabatic assumption gives the liquid–water mixing ratio m_l (mass of liquid water per mass of dry air, g kg^{-1}) at a height z within the cloud as

$$m_l(z) = m_v(z_b) - m_v(z), \tag{3}$$

where m_v (g kg^{-1}) is the water-vapour mixing ratio and z_b (m) is the cloud-base height. A parcel of moist air rising from underneath the cloud reaches saturation at the cloud base z_b. On its way up within the cloud, no moisture is removed from or added to the parcel.

For clouds with such an adiabatic profile, Brenguier *et al.* (2000) state a relationship of liquid–water path W with the square of cloud thickness, based on considerations presented by Boers and Mitchell (1994). This implies that for adiabatic clouds, thickness can be approximated using the liquid–water path. In the absence of liquid–water path information, Minnis *et al.* (1992) and Heidinger and Stephens (2000) use cloud optical thickness τ as a proxy value and fit its distribution to observed marine stratocumulus thickness data (see figure 2 for a comparison).

While these parameterizations have a certain validity for approximating cloud systems closely resembling the ones they were fitted to, their transferability has to be questioned (as shown in Bendix *et al.* 2005). In these approaches, a low optical thickness is interpreted as a low geometrical thickness, while it may as well indicate a low droplet size (e.g. in a thick cloud with little pollution). As shown in equation (4), the relationship between optical depth and liquid–water path is via droplet effective radius. The use of τ alone as a proxy for W therefore has to be questioned

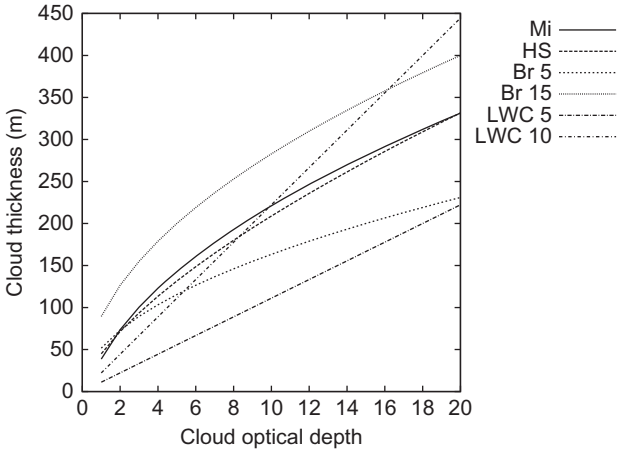

Figure 2. Geometrical thickness retrieved using a range of approaches presented in the text. Mi: Minnis *et al.* (1992), HS: Heidinger and Stephens (2000), Br: Brenguier *et al.* (2000) using a cloud-base temperature of 273 K and the droplet effective radius indicated (5 and 15), LWC: using a fixed liquid–water content of 0.25 g m^{-3} and the droplet effective radius indicated.

$$a_e \cong \frac{3W}{2\rho_l \tau}, \tag{4}$$

where ρ_l is the density of liquid water (g m^{-3}) and a_e is the droplet effective radius (μm).

Other authors further explore the adiabatic cloud model with respect to liquid–water content and liquid–water path. In an adiabatic cloud, (adiabatic) liquid–water concentration ρ_c^{ad} and height z above cloud base z_b are related linearly. For thin low-level clouds, the adiabatic cloud liquid–water path (g m^{-2}) is given by

$$W^{ad} = \frac{C_w \Delta_z^2}{2}, \tag{5}$$

(Brenguier *et al.* 2000), where C_w (g m^{-3} m^{-1}) is the moist adiabatic condensate coefficient and describes the rate of change of liquid water with height.

On the assumption that a liquid–water path retrieved from satellite data as presented above represents an adiabatic cloud, Δ_z can be computed using this relationship. Iwabuchi and Hayasaka (2003) apply this insight to the retrieval of boundary-layer cloud geometrical thickness. An evaluation by Bendix *et al.* (2005), however, has shown this technique to perform very poorly for low stratiform clouds, implying that the adiabatic assumption is incorrect for this type of cloud.

2.3 *Pseudosounding*

A third strand of approaches designed to retrieve cloud geometrical thickness makes use of the asymptotic absorption limits in the middle infrared (usually around 1.6 or 3.9 μm). In this range, photon absorption increases with wavelength. This means that a radiation originating from a cloud is more likely to be absorbed at longer mid-infrared (MIR) wavelengths, so that the information contained in satellite-received radiation represents increasingly shallow layers at cloud top (Platnick 2000).

Satellite-based retrievals of cloud optical properties generally foot on a homogeneous plane-parallel cloud (vertically uniform plane-parallel) model. This concept assumes a cloud with no vertical (and horizontal) variation. Ideally, the microphysical parameters retrieved at different MIR wavelengths should therefore be identical. In a real cloud, droplet effective radius varies with height. Therefore, given the differences in MIR penetration depths, conclusions regarding the vertical profile of the cloud are possible (Bendix *et al.* 2005). This technique is referred to as 'pseudosounding'.

Unfortunately, properties observed at different MIR wavelengths represent the cloud at different optical, rather than geometrical, depths (Chang and Li 2003). Therefore, no information on cloud geometrical thickness can be derived from multiple-wavelength MIR measurements alone.

The only way to resolve a geometrical cloud profile from different MIR optical penetration depths is by fitting the distribution to an assumed vertical-cloud profile. This is done by various authors using adding-and-doubling radiative transfer models (e.g. Platnick 2000, Chang and Li 2002a,b, 2003, Schüller *et al.* 2005), mostly using adiabatic assumptions.

While this type of technique is very well rooted in cloud radiative physics, and may be expected to produce results of good accuracy, its applicability to fog thickness retrieval using MSG SEVIRI is limited by the channels available on this system (1.6 and 3.9 μm). At 1.6 μm, clouds of optical depths less than 15 are fully penetrated (Platnick 2000), so that no significant vertical signature will be found.

3. Methodology

As seen in the literature review presented in the previous section, none of the techniques commonly used in cloud-thickness retrieval shows much promise for low-stratus retrieval from SEVIRI data. The main problem with the approaches outlined above is that the actual distribution of liquid water within the cloud is poorly approximated. Therefore, a new method is introduced here with an explicit model of cloud liquid–water distribution. Some considerations regarding vertical distribution of liquid water in fog and low stratus are presented, followed by a description of the cloud-model design.

3.1 *Vertical stratification of fog and very low stratiform clouds*

While the more sophisticated approaches presented above generally assume linear profiles of cloud microphysical parameters, the buildup of real clouds is more complex. The adiabatic increase in liquid–water content with height is a rare exception; most clouds have distinctly sub-adiabatic profiles, that is, water content increases more slowly. Indeed, data presented by Brenguier *et al.* (2003) clearly show that an adiabatic profile of ρ_c systematically overestimates the real liquid–water path. The development of a more realistic cloud-thickness retrieval technique therefore requires a closer consideration of vertical water distribution in fog.

As a measure of departure from the adiabatic situation, Betts (1982) introduced the in-cloud mixing parameter

$$\beta = \frac{\mathrm{d}p_s}{\mathrm{d}p}, \tag{6}$$

(Betts 1982), where p_s is the saturation pressure (i.e. the point where a parcel just reaches saturation) at pressure level p. For a well-mixed layer, the saturation point is constant, yielding $\beta = 0$ for adiabatic situations (saturation is reached at cloud base). For sub-adiabatic clouds, β typically takes values $0 \leq \beta < 1$. A departure from $\beta = 0$ impacts on liquid–water concentration

$$m_l(z) = (1 - \beta) m_l^{ad}(z), \tag{7}$$

(Boers and Mitchell 1994), where $m_l(z)$ is the liquid–water mixing ratio at height z and $m_l^{ad}(z)$ (g moisture/kg dry air) is the adiabatic liquid–water mixing ratio at the same level. Thus, for small β, the water mixing ratio remains close to adiabatic; when β approaches 1, liquid water falls to 0.

In a number of studies, average mixing parameters between 0.3 and 0.4 have been identified for boundary-layer stratocumulus clouds, and slightly lower values for stratus (Slingo *et al.* 1982, Boers and Betts 1988, Betts and Boers 1990, Boers *et al.* 1991, Boers and Mitchell 1994).

For the purpose of cloud geometrical thickness determination in the context of the present study, the processes in vertical cloud development deserve closer consideration. In particular, the processes of cloud formation and development need to be reconsidered in this light.

Generally, droplets in stratiform clouds, including fog, form by condensation rather than by coalescence. Turbulent mixing is of minor importance. The formation of radiation fog presents a special situation since it occurs at the ground surface. Nonetheless, the dominant processes effecting liquid–water distribution within a boundary-layer stratiform cloud are very similar.

As a special case, radiation-fog development will be considered in the following paragraphs. Where applicable, parallels to other very-low-stratus clouds will be shown. The formation and development of radiation fog involves a fine balance of radiative cooling and turbulent mixing of air. It can be split into three main processes, each with a distinct impact on water distribution within the cloud. These processes are presented in overview in figure 3. Development stages in this figure are labelled in agreement with the following paragraphs:

(1) Radiative cooling takes place at the ground surface. At this stage, slight turbulence is needed to spread the cooling effect to and within the air near the ground. Condensation sets in. Initially, the condensate is deposited on the ground as dew, due to the prevailing turbulence. The further development of fog in this situation depends on comparatively calm conditions, that is, the initial turbulence must subside so the water loss due to dew settling ceases (Brown and Roach 1976, Roach 1995). Only very slight turbulence (up to 0.5 m s^{-1}) still occurs at this stage (Gerber 1981). Radiative cooling then leads to thickening and stabilization of the fog layer as the cooling surface moves upwards.

Liquid–water content in the cloud rises with height in the fog layer (Pruppacher and Klett 1997). Because there is little vertical motion within the cloud, the droplet number concentration remains almost constant with height. Increasing liquid–water content manifests itself in increasing droplet size (Brenguier *et al.* 2000, Chang and Li 2002b).

The liquid–water profile at this stage is sub-adiabatic by tendency, as shown in the first panel of figure 3.

(2) Heat conduction from the soil continues after the radiatively cooled surface has shifted upwards, resulting in heat and moisture convection into the lower fog layers (Roach 1995). Mixing thus sets in again at the fog base.

For all boundary-layer clouds, with or without ground contact, layer coupling, that is, exchange between layers, is generally better (i.e. β smaller) in the presence of strong and low inversions (Durand and Bourcy 2001). Also, a good coupling of the lowermost cloud layer to the air layer near the surface (where not in contact with the ground) reduces local in-cloud β to values near 0. Water supply from below the cloud is steady and mixing conditions near the cloud base are close to adiabatic. Meyer and Rao (1999) use $\beta = 0.1$ for this region.

This influence of the ground or the layer below the cloud is shown in the second panel of figure 3.

(3) Radiative cooling of the upper fog layers leads to convective turbulence within the fog (Caughey *et al.* 1982). This process has two main effects: on the one hand, the resulting upward movements of moisture within the cloud enhance the increase of water content with height (Oliver *et al.* 1978, Manton 1983, Walker 2003). On the other hand, water content near the cloud top is depleted due to dry-air entrainment (Roach 1995). The cloud-top layer is quickly decoupled from the lower layers; the monotonical rise in liquid–water content thus stops just below the cloud top. Dry air from the surroundings is mixed into the cloud leading to a quick decline in droplet size and water content (Brown and Roach 1976, Roach *et al.* 1982, Driedonks and Duynkerke 1989, Hoffmann and Roth 1989, Boers and Mitchell 1994). This point is usually reached at about 80–90% of cloud height (Wieprecht *et al.* 2005).

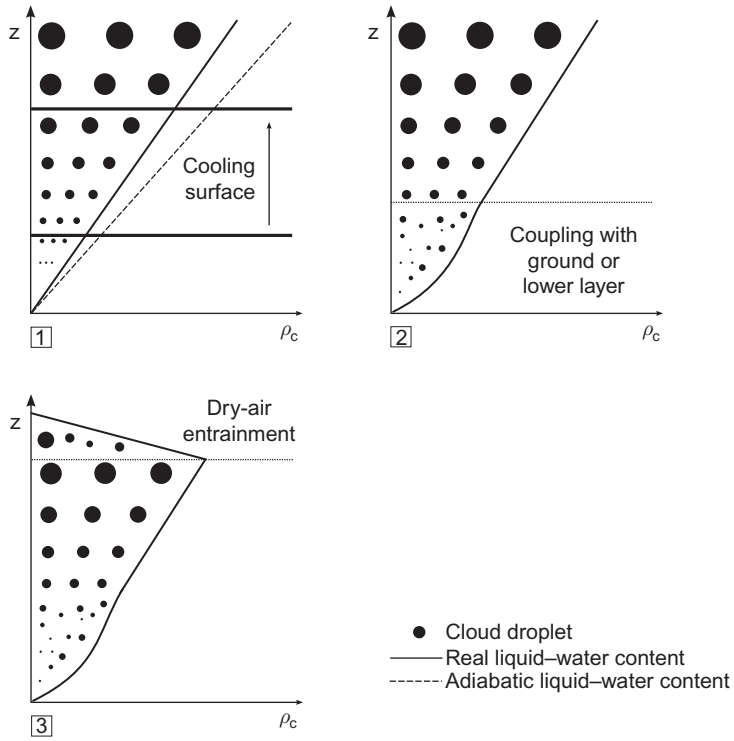

Figure 3. Processes in fog and very-low-stratus development. For a detailed description, see text; development stages are numbered like the corresponding paragraphs.

For very-low-stratus clouds other than radiation fog, cloud development obviously does not start at the ground, so that initial cloud formation follows a different pattern. However, the parallels in cloud development and stratification are extensive. As in radiation fog, turbulence is of minor importance or largely absent in the formation process. Coupling with the layer below the cloud and cloud-top entrainment take place in elevated very-low-stratus clouds as well, so that the resulting cloud profile is very similar to the one described above and depicted in figure 3.

The idealized profile described in the above paragraphs is closely matched by observations of fog and very low stratus. Detailed descriptions of the processes and corresponding measurements in fog and very low stratus are also given in a large number of studies (e.g. Best 1951, Caughey *et al.* 1982, Fitzjarrald and Lala 1989, Hayasaka *et al.* 1995, Heintzenberg *et al.* 1998, Hess *et al.* 1998, Genio and Wolf 2000, Miles *et al.* 2000, Platnick 2000).

3.2 *Model concept and design*

The new method for cloud-thickness retrieval was designed to closely follow the cloud-profile and cloud-process considerations presented above.

Figure 4 gives an overview of the new scheme. Liquid–water path and cloud-top height are known for a given pixel; they are retrieved according to the methods described in Kawamoto *et al.* (2001, liquid–water path) and Cermak (2006, cloud

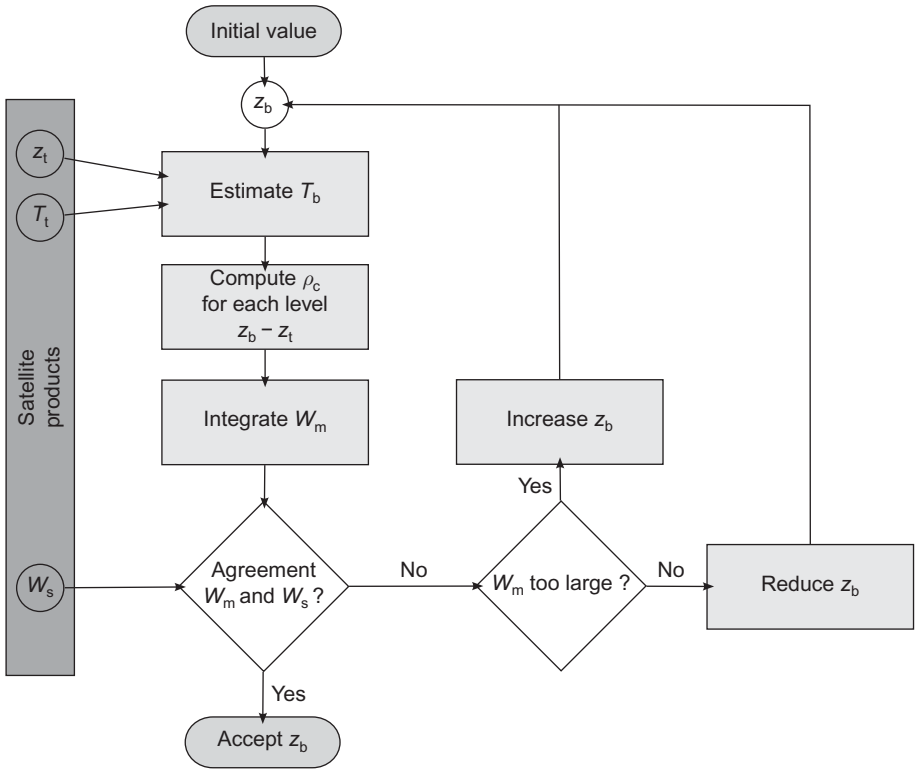

Figure 4. Overview of the cloud-base height retrieval scheme. See text for an explanation of the procedure. W_m: liquid–water path from cloud model, W_s: liquid–water path from satellite data, T_t: cloud-top temperature, z_t: cloud-top height, T_b: cloud-bottom temperature, z_b: cloud-bottom height, ρ_c: cloud liquid–water content.

height). Cloud-water distribution is simulated for clouds with the known cloud-top height and assumed cloud-base heights. This procedure is repeated iteratively until liquid–water path of the modelled cloud agrees with the liquid–water path retrieved from satellite imagery. The corresponding cloud-base height is accepted as the valid assumption for the given pixel.

The main challenge in model development is to accurately quantify the deviation from the adiabatic profile, that is, the mixing parameter β. A number of values for β have been reported by various authors (see above). However, in the light of the very-low-stratus development processes discussed above, a more detailed consideration of the cloud profile is warranted. Therefore, in the newly developed model, the cloud is considered as consisting of three layers with different values of β. For each cloud layer from an assumed cloud base to the known cloud top, the adiabatic liquid–water content is computed and then modified according to β assumed for the layer

$$\rho_c(z) = (1 - \beta)\rho_a m_l(z), \tag{8}$$

where ρ_a is the density of air and $m_l(z)$ (g kg^{-1}) is the liquid–water mixing ratio at height z (equation (3)). $m_l(z)$ is a function of pressure and temperature at z.

The parameterization of β for each layer closely follows the discussion of cloud processes presented above. The cloud is segmented into three layers, cloud top

(entrainment), cloud base (coupling with ground or surface layer) and the region in between. The concepts introduced in the following paragraphs are visualized in figure 5.

- In the central region of the cloud (between the base and top layers), a fixed value of β is applied. It has been stated above that coupling of cloud layers is greater the closer a cloud is to the ground. β is therefore scaled from 0 to 0.3 according to cloud-top height above ground, with

$$\beta = \frac{0.3 z_t}{1000}. \tag{9}$$

  In this way, a cloud with top height $z_t = 1000$ m will be assigned a β of 0.3, a cloud with $z_t = 500$ m will be assigned a β of 0.15. This figure is then fixed for the central cloud region.
- On the assumption that moisture is fed into the cloud from below (see above), β must be smaller in the lower part of the cloud and gradually increase towards the central region. Within the lowermost 75 m of the cloud β_1 (β of the lowermost layer) is scaled linearly from 0 to β of the central region, increasing upwards. This marks the transition from an almost adiabatic increase in ρ_c to a layer with worse coupling.
- Near cloud top, dry-air entrainment quickly reduces ρ_c to zero. To account for this in the model, where the uppermost 50 m are reached (Wieprecht *et al.* 2005), liquid water linearly drops to 0 up to the cloud top.

The integration of ρ_c over the thickness of the cloud yields modelled liquid–water path W_m. This bulk parameter is also known from satellite retrievals (W_s), so that model and measured parameters can be compared. This is done in an iterative procedure in which cloud base is shifted until the best match is found. In the first step, cloud bases at 300 m below ground and just below the known cloud top are assumed. They are iteratively raised and lowered to close in on the measured liquid–water path (see figure 4).

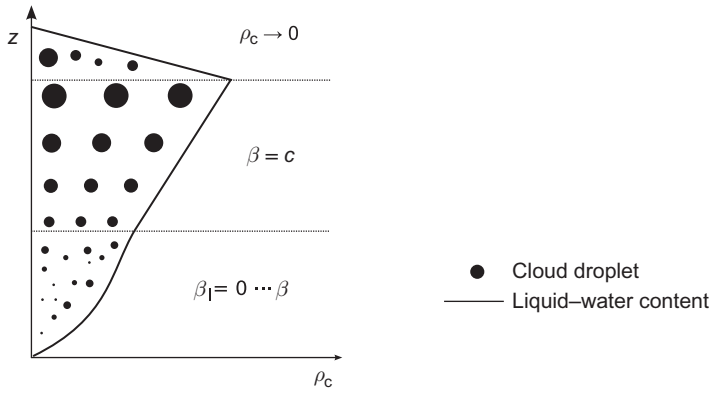

Figure 5. The cloud-profile parameterization used for cloud liquid–water path computation. The figure shows the development of mixing ratio β and liquid–water content ρ_c with height in the cloud. Cloud layers are the same as those shown in figure 3. β_1 is the adapted β of the lowermost layer, c is a constant.

Since the satellite-derived quantity of W_s is retrieved at a wavelength of 3.9 μm with a small photon-penetration depth into the cloud (see above), its value is not representative of the entire cloud. Platnick (2000) quantified the relationship between observed and retrieved W_s for several cloud optical depths. These relationships are used to correct satellite W_s before fitting the model.

While above cloud-base height was generally defined as the point where cloud liquid–water content drops to 0, the definition of fog requires a certain level of extinction, that is, a visibility less than 1000 m. Therefore, visibility is computed for each level as well. Visibility (V, in m) is derived from extinction by Koschmieder's law for a contrast threshold of 2%

$$V = \frac{1}{\beta_e} \ln\left(\frac{1}{\varepsilon}\right), \tag{10}$$

where β_e is the molecular extinction coefficient and ε is the contrast threshold (%).

Droplet effective radius a_e (μm) for each level is computed on the assumptions that a_e retrieved at 3.9 μm is the cloud-top value, cloud base a_e is at 1 μm and the intermediate values are scaled linearly in between.

The lowest height with visibility < 1000 m within the fitted profile is identified as the base of the fog layer.

The modelled cloud-base height very much depends on the validity of all the assumptions and parameterizations. In order to express this uncertainty, a ground-fog confidence level is computed. Technically, ground fog is likely to occur when the computed cloud base is at or below the surface elevation in a given location. This elevation is taken from a DEM. Negative cloud-base heights (computed cloud base below the surface) can occur due to deviations in the actual liquid–water distribution of the cloud from the modelled distribution. Ground-fog confidence levels are scaled on an interval from 0 to 1. A confidence level of 1 is assigned to situations where half of the simulated cloud or more lies below the ground surface, that is, $z_t - z_b \geq 2(z_t - z_s)$, where z_t is the cloud-top height, z_b cloud-base height and z_s surface elevation. A confidence level of 0 is given to situations where at least one cloud thickness remains between cloud base and the ground, that is, $z_t - z_s \geq 2(z_t - z_b)$. The computation of the ground fog confidence level P_g for any given z_b is as follows:

$$P_g = 0.5 - 0.72 \ln\left(\frac{z_t - z_s}{z_t - z_b}\right). \tag{11}$$

3.3 *Model sensitivities and plausibility*

A sensitivity study of the model expectedly reveals a strong dependency of simulated cloud thickness on liquid–water path and cloud-top temperature. This relationship is shown in figure 6. The thickness of warm clouds changes almost linearly with liquid–water path; the effect of small temperature changes is more enhanced at lower cloud-top temperature levels. Generally, at constant thickness, a warm cloud will have a higher liquid–water path than a cold cloud. This is very much in accordance with physical expectations.

In order to assess model plausibility, a few profiles of microphysical properties in stratus layers have been extracted from the literature and compared with model output. They are presented in figures 7, 9 and 10. The best-fit modelled profile is

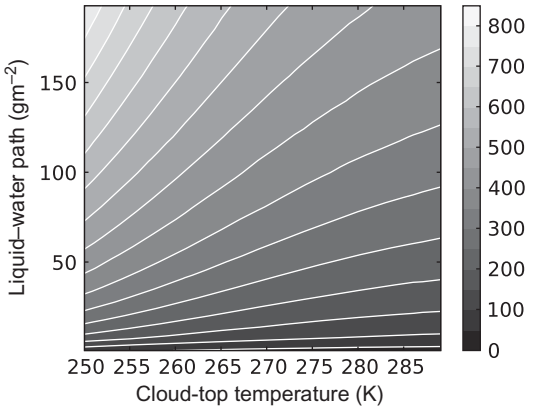

Figure 6. Dependence of simulated cloud thickness (m) on liquid–water path and cloud-top temperature, at a constant cloud-top height of 500 m above ground.

shown in each figure, along with an adiabatic profile and a horizontal line indicating cloud-base height computed from equation 5 (the 'Brenguier approach').

Figure 7 shows the liquid–water content of a low stratiform cloud reported by Slingo and Schrecker (1982). The modelled profile very well approximates the cloud dimensions, while an adiabatic profile and the Brenguier parameterization both overestimate the cloud-base height. This is a typical example of a sub-adiabatic low-stratus cloud profile as discussed above. Ground-fog confidence is at $P_g = 0.00$. This means that the new scheme classified this cloud as not touching the ground at maximum confidence.

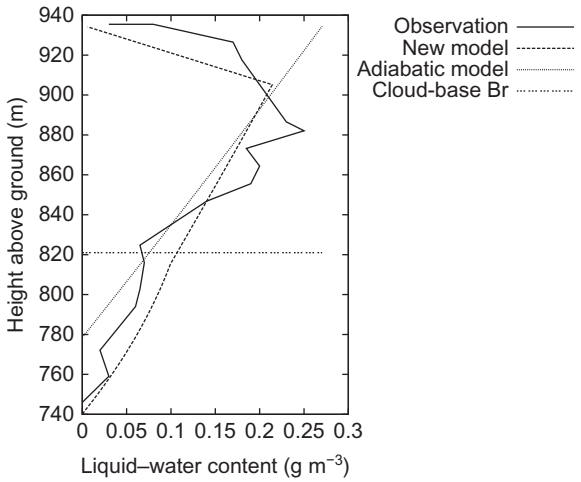

Figure 7. A low-stratus cloud profile observed by Slingo and Schrecker (1982), with a cloud base of 745 m. The profile is shown together with liquid–water content modelled using an adiabatic model, the new sub-adiabatic model and cloud-base height retrieved based on the parameterization by Brenguier (equation (5), 'cloud base Br'). For a listing of measurements and modelled values, see table 2.

This profile was also used to explore the sensitivity of cloud-base prediction accuracy to the thresholds of β and cloud-base and cloud-top transition. Figure 8 shows the deviation of the modelled profile from the measured cloud thickness as a function of the chosen value of β, the height of the cloud-base transition zone and the cloud-top zone. It can be seen that with increasing β, cloud-base height is underestimated. This is because at a larger β, the same liquid–water path fills a thicker cloud. Increasing the height of the cloud-base transition zone, that is, the zone in which β_1 is scaled from 0 to β, generally effects an overestimation of cloud-base height. When the height of the cloud-top transition zone, that is, the zone where cloud liquid–water content drops to 0, is increased, cloud-base height is underestimated by tendency. Overall, these figures show that the thresholds deduced from the literature review ($\beta = 0.3$, cloud-base transition = 75 m, cloud-top transition = 50 m) very appropriately approximate the profile considered.

A description of a ground-fog profile from the literature is given in Pinnick *et al.* (1978). Unfortunately, these authors only measured the profile up to a height of 155 m above ground, while their measurements clearly indicate that the cloud top is not yet reached at this height (liquid–water content $\gg 0$). The remaining part of the profile is thus estimated as shown in figure 9. The Brenguier parameterization underestimates cloud thickness and thus does not identify it as a cloud with ground contact. On the other hand, both models overestimate the profile, even the adiabatic model. This is due to the fact that there is no real cloud base. In order to understand the model thickness overestimation it needs to be considered that the fog profile starts with a liquid–water content of almost 0.1 g m^{-3} at the surface, which is only possible in situations with cloud–ground contact. The models, however, assume a cloud-base water content of 0, so that, naturally, the modelled cloud base must be below the surface. For this example, the overestimation of the thickness is not a problem as ground contact is properly detected. A sound ground-fog confidence of $P_g = 0.70$ is computed for this profile based on equation (11).

A more critical situation arises when this fog layer is lifted from the ground. The process of fog 'lifting' involves a significant depletion of cloud liquid–water content. Beginning in the lowermost part of the fog, radiative cooling ceases and heat flux from

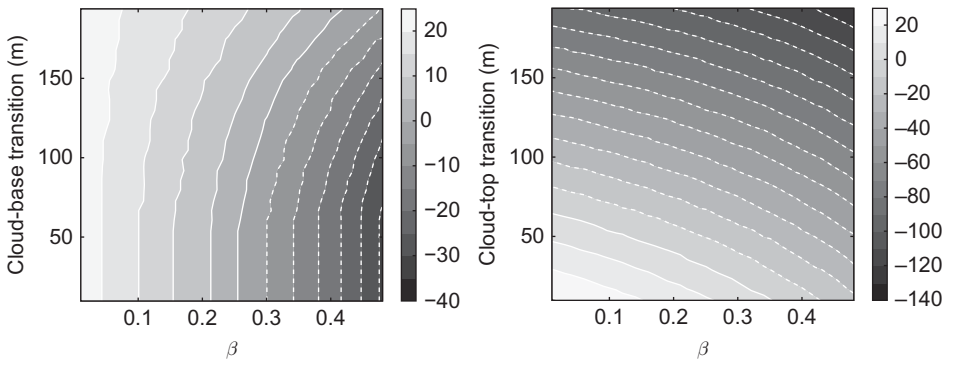

Figure 8. Deviation of the computed cloud-base height from observed cloud-base height in metres as a function of β, cloud-base transition and cloud-top transition. For a constant β, increasing the height of the cloud-base transition zone leads to increasing overestimation of cloud base (left-hand panel). The dependence on β is very strong. Increasing the height of the cloud-top transition zone leads to enhanced underestimation of cloud base.

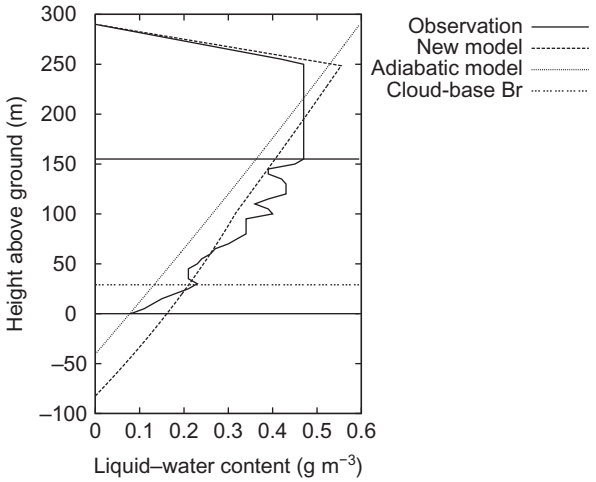

Figure 9. A ground-fog profile taken from Pinnick *et al.* (1978). For explanations, cf. figure 7. The thin horizontal lines indicate the upper and lower limits of the original data. For a listing of measurements and modelled values, see table 2.

the ground serves to evaporate fog droplets (Roach 1995). An example of such a situation of a fog layer lifted to a small height above ground is shown in figure 10. These data are extracted from Pinnick *et al.* (1978). Again, there are no data above 155 m; it was assumed that liquid–water content above this height linearly drops to 0 within a further 30 m. In agreement with the prediction stated above, this lifted profile is clearly sub-adiabatic and thus adequately approximated by the model. Ground-fog confidence is at $P_g = 0.23$. The adiabatic model and parameterization, on the other hand, underestimate cloud thickness.

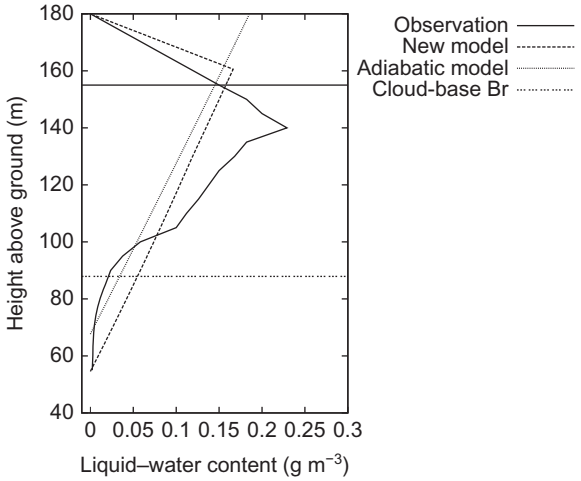

Figure 10. A profile of uplifted fog as reported by Pinnick *et al.* (1978) with a cloud-base height of 57.5 m. Explanations in figure 7. The thin horizontal line indicates the upper limit of the original data. For a listing of measurements and modelled values, see table 2.

Table 2. Comparison of cloud-base heights for the profiles presented in figures 7, 9 and 10 by different methods.

Profile (figure)	W (g m^{-2})	Cloud base observed (m)	Deviation new model (m)	Deviation adiabatic (m)	Deviation Brenguier (m)	Ground-fog confidence
7	22.0	745	–4	–24	+76	0.00
9	99.0	0	–92.5	–60.5	+29	0.70
10	10.8	57.5	–1	+12	+30.5	0.23

The results of all three profiles discussed are summarized in table 2. Based on these profiles and the considerations presented in conjunction with them, it can be presumed that the sub-adiabatic profile assumption used in the new model is valid for ground fog, low-stratus clouds and lifted fog layers. The thickness of ground-fog patches may be overestimated; however, this is not critical, as ground contact of the layer will still be predicted accurately in these situations. Based on the profile analysis discussed here, overall performance of the new model is expected to present a marked improvement over adiabatic assumptions.

4. Application and validation

In order to appraise the performance of the scheme, an extensive validation study was conducted. First, data selection and methodology are discussed, followed by a presentation of validation study results.

4.1 *Fog detection and data selection*

The area covered by fog is retrieved in a three-step procedure: first, the spatial extent of fog and low stratus is derived using the well-validated technique described in Cermak and Bendix (2008), using a combination of spectral and spatial tests. Then, cloud liquid–water path and cloud-top height are retrieved from the SEVIRI data according to the methods described in Kawamoto *et al.* (2001, liquid–water path) and Cermak (2006, cloud height), before cloud base height is modelled. The channels used in each product are summarized in table 1. The liquid–water path retrieval uses a combination of an absorbing (3.9 μm) and a non-absorbing (0.6 μm) channel to infer optical thickness, droplet effective radius and liquid–water path of a cloud. The look-up table used for this is based on radiative-transfer calculations. Surface reflectance is included in the scheme.

Cloud-top height is retrieved in two different ways, depending on the situation of the cloud. In areas where the cloud is limited by terrain, the altitude of the pixels surrounding the cloud is extracted from a DEM and interpolated across the cloud area. Where this is not possible, a temperature lapse rate is applied to estimate the height of each cloudy pixel. The scheme includes various corrections of cloud-top temperature and land-surface temperature (including water-vapour correction, following Sobrino and Romaguera 2004), as well as an interpolation of land-surface temperature for the area underneath the cloud and automatic lapse-rate extraction. Full details can be found in Cermak (2006).

On the basis of low-stratus area and properties as described in the above paragraphs, fog presence is detected using the cloud model and equation (1).

The satellite data set used for the validation study needs to meet a few requirements in order to allow a reasonable interpretation. The ideal satellite product data set:

- Features a great range of atmospheric and cloud situations, allowing for a thorough assessment of the algorithm's skill in separating low cloud from higher cloud layers.
- Includes numerous different low cloud situations, so that the accuracy of ground-fog detection can be tested.
- Covers all daytime hours.

It is highly unlikely that all three conditions will be met in a random set of satellite scenes, unless an extremely large sample is selected. Therefore, the validation data was chosen based on visual inspection. The sole criteria in the selection process were the requirements given above.

The satellite product data set chosen for validation consists of 1030 MSG SEVIRI scenes. They cover 24 days in three periods, 20–22 September, 7–21 October and 5–10 November 2005. Within the test data set, all available scenes were considered without prior selection. With 1030 scenes, this data set is very extensive, covers a large range of meteorological situations and is thus very well suited for quantitative evaluation. The presence of ground fog was tested against visibility measurements in the reference data set, with ground fog defined as a situation with a visibility of up to 1000 m. On the satellite side, all predictions with a ground-fog confidence level P_g of 0.5 or greater were considered ground fog. As cloud-geometry computation is only implemented for clouds previously identified as very low stratus, the validation statistics consequently include only these cases.

The general target of a validation study is to assess the validity of a technique, that is, its agreement with reality. In the particular case of an operational satellite-based product with spatially relevant results, the following requirements must be met by a reference data set used in validation:

- Validity/reliability. A reference data set needs to be of trusted and operational quality.
- Good spatial coverage. Ideally, the entire study area should be covered with reference data evenly distributed.
- Appropriate temporal resolution. In order to track change over time, reference data should be available at a frequency of 1 hour or better.

Station measurements of ceiling and visibility are available globally in the processed form of METeorological Aerodrome Reports (METAR) at hourly intervals. All 583 stations available in the study domain are included in the reference data set used.

For each data point in the reference data set, a corresponding value was extracted from the satellite product based on the ground-station co-ordinates. Since the fog-detection technique works during daytime only, pixels with solar zenith angles larger than 80° were excluded. This limitation is inherited from the microphysics retrieval.

4.2 *Validation methodology*

Validation of the satellite fog-detection method is performed using a number of confusion-matrix-based statistical indices. These are documented in the literature (e.g. Marzban 1998). As a service for the interested reader, an overview of the relevant indices is given at the end of this section.

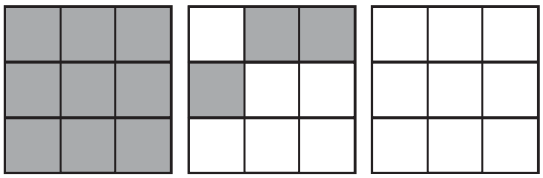

Figure 11. A 3×3 pixel environment covered by fog (grey fill) to varying degrees. If ground-based measurements indicate fog, situations with any fog detected by the satellite in the 3×3 pixel environment (left and centre panels) would be classified as hits, whereas the panel on the right-hand side would be a miss.

Collocation between the satellite pixel and the ground-based assessment can be an issue because often both measurements are taken at different points in time; also, a station may lie between two pixels. In order to compensate for this, all indices were computed not only for individual pixels, but also for a 3×3 pixel environment (around 16.5 km × 9.5 km in Europe). This approach is based on the assumption that the sought-after ground station might be represented in one of the pixels neighbouring the one identified as the theoretical location. Each 3×3 pixel environment was therefore tested for the presence of the feature found in the corresponding ground station data. Where any one of the pixels agreed with the reference measurement, it was taken to be the sought-after location. Thus, for instance, a hit would be observed when, for a fog observation in METAR, any satellite pixel in the 3×3 matrix indicates fog. Figure 11 illustrates this principle. Since this approach is somewhat biased, both the pixel-based and the 3×3 approaches are presented. A more extensive treatment of possible sources of uncertainty in comparing satellite and ground-based data can be found in Cermak and Bendix (2008).

Contingency tests. The skill of a forecast or classification is defined as the improvement over an uninformed random prediction (Briggs and Ruppert 2004). A range of scalar contingency test indicators have been proposed, applied and evaluated (e.g. Doswell *et al.* 1990, Murphy 1993, Brooks and Doswell 1996, Marzban 1998, Wright and Thomas 1998, Stephenson 2000, Zhang and Casey 2000, Thornes and Stephenson 2001, Baldwin and Kain 2004, Wilson and Burrows 2004). Out of these, a selection was made here based on their specific information content and successful application in similar studies.

The basis of all indicators is a 2×2 confusion matrix showing agreement and disagreement in the dichotomous classification to be tested and reference data set (table 3). In this table, A gives the number of correctly predicted instances of the property (hits), B false alarms (property predicted but not present), C misses (property present but not predicted) and D correct negatives. The sum of all columns and rows $A + B + C + D = n$ is the total size of the sample.

Table 3. Confusion matrix.

	Observation yes	Observation no
Prediction yes	A	B
Prediction no	C	D

Notes: A: correctly identified situations (hits), B: false alarms, C: misses, D: correct negatives.

Table 4. Statistical indicators used in this study, with computation, theoretical range of values and best value (for a maximum skill prediction).

Name, information	Equation	Range	Best
Bias score (over-/underestimation)	$BS = \frac{A+B}{A+C}$	$0 \cdots \infty$	1
Hit rate (correct identification)	$HR = \frac{A}{A+C}$	$0 \cdots 1$	1
False-alarm rate (false identification)	$FAR = \frac{B}{A+B}$	$0 \cdots 1$	0
Threat score (overall skill, robust)	$TS = \frac{A}{A+B+C}$	$0 \cdots 1$	1
Hanssen–Kuipers discriminant (overall skill)	$HKD = \frac{A}{A+C} - \frac{B}{B+D}$	$-1 \cdots 1$	1

For each comparison data set, a table of this kind is computed. The statistical indicators are calculated based on the values A to D, as detailed in table 4.

4.3 *Study results and analysis*

Tables 5 and 6 summarize the statistical results. Since the 3×3 pixel approach may return a result even if the central pixel is a missing data point (see previous section), the total size of this sample is greater than the single-pixel sample. In the tables, the 3×3 pixel environment displays a much better skill. The bias score points to a slight overestimation of ground-fog situations for the single-pixel approach. However, the combination of hit and false-alarm rates reveals a significant under-detection coupled with high levels of false alarms. This is also expressed in the low threat score of 0.26.

The poor skill obtained in the single-pixel approach can probably be attributed to small-scale variations in surface elevation. The ground-fog confidence level is obtained by comparing computed cloud-base height with a surface-elevation value extracted from a DEM at the spatial resolution of SEVIRI. However, the averaged elevation value for each of these pixels is unlikely to agree with the actual station elevation, leading to misestimations of ground-fog presence.

Table 5. Statistical summary of the ground-fog validation study for the single-pixel approach and the 3×3 pixel environment (see text), using elevation data from a DEM at satellite spatial resolution. Results based on a ground-fog confidence level of 0.5.

Indicator	1 pixel	3×3 pixels
BS	1.53	1.02
HR	0.52	0.74
FAR	0.66	0.27
TS	0.26	0.58
HKD	0.52	0.74

Notes: BS: bias score, HR: hit rate, FAR: false-alarm rate, TS: threat score, HKD: Hanssen–Kuipers discriminant.

Table 6. The confusion matrix behind the indices in table 5, 1/3×3 pixel approaches.

	Validation: fog	Validation: no fog
Satellite: fog	108/143	208/53
Satellite: no fog	99/50	69344/76257

Accordingly, the 3×3 pixel approach yields much better results. At constant accuracy, the threat score now more than doubles (0.58), the hit rate reaches a satisfactory 74% and the false-alarm rate drops to 27%.

In the light of these findings, a more appropriate approach to ground–satellite intercomparisons may be the use of individual station elevation data instead of the averaged satellite-scale DEM. In this approach, the ground-fog confidence level is computed using satellite-derived cloud-base height and the surface elevation of the respective METAR station. The statistical indicators were thus recomputed using these station-specific confidence levels, again with a cut-off level of $P_g = 0.5$. The results are presented in tables 7 and 8.

The most obvious change is an increase in the hit rate in both the single-pixel and 3×3 pixel approaches. The overall quality of the former changes only very little as indicated by the threat score and Hanssen–Kuippers discriminant (HKD). This is due to an increased false-alarm ratio. For the 3×3 pixel environment, results have improved, however. At a constant false-alarm rate, the hit rate has risen by seven points to 81%.

A portion of the false alarms may possibly be explained by the wind speed near the ground: where this parameter is too large, fog cannot persist directly at the ground surface, although it may still be present at very low elevations. The average wind speed reported by METAR stations for the correctly identified ground-fog situations is 1.5 m s^{-1}, with a standard deviation of 1.3. For false alarms, that is, situations incorrectly classified as ground fog, average wind speed reaches 3.2 m s^{-1}, more than one standard deviation in excess of mean ground-fog wind speed. It thus seems plausible that local variations in wind conditions very near the ground may indeed alter the visibility conditions at the surface. The small changes produced by this process are not detected by the satellite sensor, leading to false alarms.

The large number of correct negatives leads to an increase in the HKD to 81%. The overall threat score now reaches 0.62, showing that good skill can be expected from the ground-fog detection scheme.

Table 7. Statistical summary of the ground-fog validation study for the single-pixel approach and the 3×3 pixel environment (see text), using real elevation data for each ground station.

Indicator	1 pixel	3×3 pixels
BS	2.03	1.11
HR	0.56	0.81
FAR	0.72	0.27
TS	0.23	0.62
HKD	0.56	0.81

Notes: Results are based on a ground-fog confidence level of 0.5. Abbreviations and acronyms as in table 5.

Table 8. The confusion matrix behind the indices in table 7, 1/3×3 pixel approaches.

	Validation: fog	Validation: no fog
Satellite: fog	112/204	293/76
Satellite: no fog	88/49	79093/84356

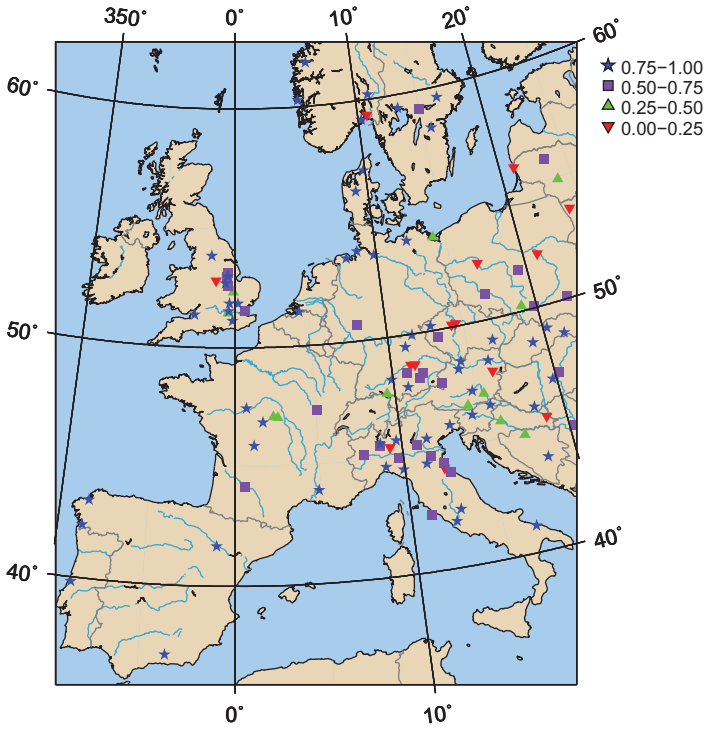

Figure 12. Threat scores by station for the validation study period (3×3 pixel approach) for ground-fog presence. Only stations with ground-fog reports in the validation study period are shown.

The distribution of threat scores in the study region is shown in figure 12. Only stations with ground-fog reports in the validation study period are shown. No clear regional pattern can be detected, indicating that the skill level is approximately even throughout the study area. Some of the smaller threat scores are at or near river courses, and thus possibly in varied relief. But the data do not allow for any definite conclusions in this regard.

In the validation statistics presented above, a cut-off ground-fog confidence level of 0.5 was used. The reason behind this choice is that 0.5 is defined as the level where cloud-base height and surface elevation match. In order to assess the changes incurred by varying this threshold, statistics were also computed for other cut-off levels. The variation of hit and false-alarm rates with changes in threshold was explored in more detail. Figure 13 shows the variation in hit and false-alarm rates for a range of ground-fog confidence levels in a variation of a receiver-operating characteristic (ROC) curve (Marzban 2004, Wilson and Burrows 2004).

Generally, proximity to the upper left-hand corner of the plot indicates increasing skill of a classification. The positions of points in the plot very clearly show that scheme performance with varying probability levels is a trade-off between hit and false-alarm rates, as one increases with the other. In this case, the classification remains well above the zero skill line for all probability levels plotted (as shown in the plot), indicating that the ground-fog classification scheme is of reliable quality. The application of a ground-fog probability cut-off level of 0.5 appears appropriate in this context.

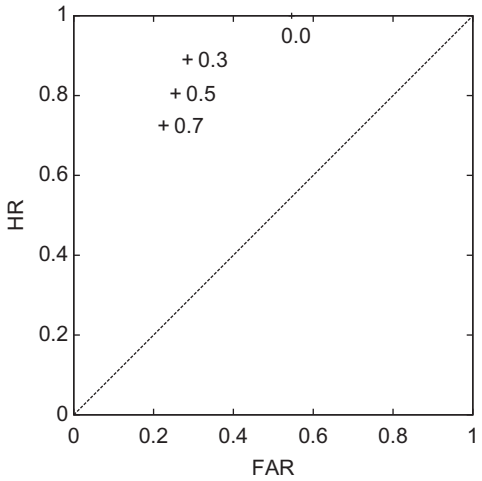

Figure 13. The skill of the fog detection algorithm at different ground-fog confidence levels (indicated by the numbers next to the data points). Skill is plotted as a function of false-alarm rate (FAR) and hit rate (HR). Numerical labels are fog confidence levels. The diagonal line represents a hypothetical forecast with no skill.

4.4 *Discussion of uncertainties*

The results of the validation study presented above need to be interpreted with care and against the backdrop of the sensitivities to and uncertainties in the assumptions and parameters on which the model rests. The assumptions in the model have been discussed above, together with their sensitivities. The main external parameters used as input for the model are cloud-top height and cloud liquid–water path. Figure 14 shows the sensitivity of retrieved cloud thickness to these two parameters for a selected case. As the figure shows, computed cloud thickness is increasingly sensitive to liquid–water path at higher cloud altitudes and where liquid–water path is small.

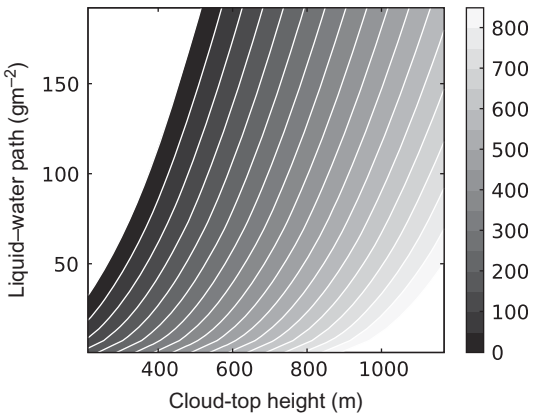

Figure 14. Dependence of simulated cloud thickness (m) on cloud-top height and liquid–water path for a selected case. Ground elevation, cloud-top temperature and ground-surface temperature are kept constant (0 m, 275 K, 273.15 K).

The dependency on cloud height is about constant with liquid–water path changes, with only slightly higher sensitivities for large values of liquid–water path.

Given these dependencies, the performance of the algorithm presented above may, in part, be due to inaccuracies in liquid–water path or cloud-top height. An explicit validation of these parameters is beyond the scope of the current article. For the microphysics scheme, Nauss *et al.* (2005) have extensively documented the performance. Liquid–water path retrievals using this method were shown to be in good agreement with comparable techniques; a positive bias of around 5% in liquid–water path was observed when contrasting the Moderate Resolution Imaging Spectroradiometer (MODIS) implementation of the product with the standard liquid–water path product available for the same platform. For typical fog liquid–water path values (10–100 g m^{-2}) this would translate to a few (0.5–5 g m^{-2}).

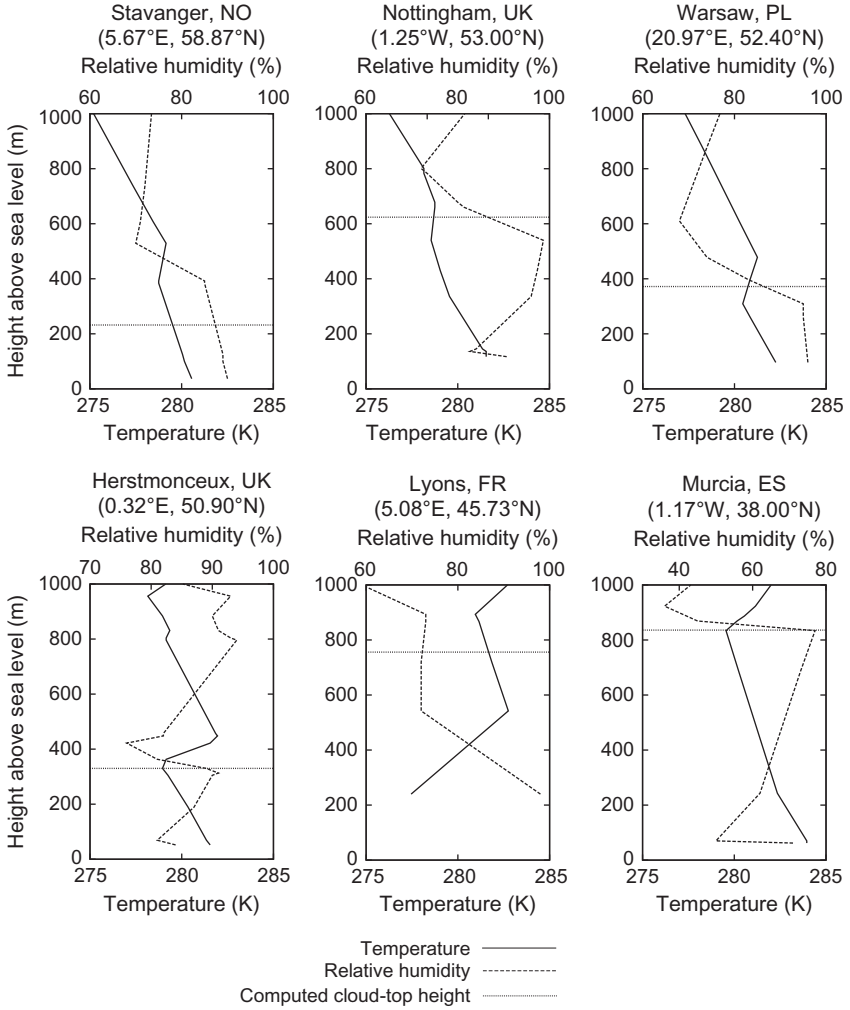

Figure 15. Radio soundings of temperature (solid lines) and humidity (dashed lines) for 1200 coordinated universal time (UTC), 16 January 2005, with cloud-top heights computed from satellite imagery.

Similarly, Cermak (2006) documented the cloud-top height retrieval. However, validation and improvement of the latter is ongoing; as a rough assessment of method plausibility, the computed cloud-top heights were compared with a series of radiosonde measurements. Figure 15 shows a selection of temperature and humidity radio soundings for 1200 UTC, 16 January 2005, throughout the study region. While radiosonde measurements offer no precise data on cloud-top height, a possible range for this parameter can be read from vertical temperature and humidity profiles. The inversion base is found where temperature begins increasing with height. The cloud top is located somewhere near this point, and is generally linked with decreasing levels of relative humidity. The satellite-derived cloud-top heights shown in figure 15 generally fall within this range around a temperature inversion base. In a quantitative evaluation of a very similar technique, Bachmann and Bendix (1993) found an average deviation of 36 m.

5. Conclusions and outlook

The validation study has provided insights into the strengths and weaknesses of the microphysics-based ground-fog detection scheme. Statistical evidence for algorithm skill has been presented. Ground-fog delineation was achieved to a satisfactory degree, with a hit rate of 81% and a threat score of 0.62. The skill of the new scheme is considerably better than a naive forecast despite misclassifications in some situations. A number of uncertainties concerning data comparability and the quality of the external input parameters complicate a strictly quantitative interpretation of the results. Nonetheless, the study has clearly highlighted the potential of the approach.

A number of challenges still remain to be addressed in future research. One point is that the current daytime-only method will be adapted for night-time application. A night-time low-stratus product for SEVIRI was recently presented by Cermak and Bendix (2007). Nighttime fog detection now requires the development of a liquid–water-path product based on infrared channel information only. Algorithm development is currently ongoing. Collaborative efforts by groups involved in ground-based and satellite-based remote sensing will produce data sets that can be used for more detailed evaluation of vertical cloud liquid–water distribution. Ongoing efforts include comparisons of liquid–water distribution as derived from cloud radar, ceilometer and radiometer measurements with satellite data. A further refinement of the microphysical model presented here and the visibility parameterization will be possible on the basis of these data sets. Also, the extension of this fog/low-stratus-centred approach to include other cloud types could become possible. Given the excellent temporal resolution of MSG SEVIRI data, a study of fog-property development is possible. Finally, the combination of passive and active sensor satellites such as in the A-train (Stephens *et al.* 2002) will be of immeasurable value for the advancement of our understanding of cloud structure. Fog situations in French Guiana are currently being investigated using such a combination.

Acknowledgements

The authors thank ESA and the European Organisation for the Exploitation of Meteorological Satellites (EUMETSAT) for early access to MSG data within the ESA MSG Principal Investigator Programme. Funding for satellite-data evaluation was provided by DFG in grants Be 1780/8-1, Be 1780/8-3 and Be 1780/14-1. European Union (EU) Cooperation in Science and Technology (COST) action 722 provided a

valuable framework for the discussion of the satellite products. The helpful comments of two anonymous reviewers are gratefully acknowledged.

References

Bachmann, M. and Bendix, J., 1993, *Nebel im Alpenraum – Eine Untersuchung mit Hilfe digitaler Wettersatellitendaten*, Bonner Geographische Abhandlungen, vol. 86 (Bonn, Germany: Ferd. Dümmlers Verlag).

Baldwin, M.E. and Kain, J.S., 2004, Examining the sensitivity of various performance measures. In *Proceedings of 17th Conference on Probability and Statistics in the Atmospheric Sciences*, Seattle, Washington, pp. 2.9.1–2.9.8 (Boston, MA: American Metrological Society).

Bendix, J., Thies, B., Cermak, J. and Nauss, T., 2005, Ground fog detection from space based on MODIS daytime data – a feasibility study. *Weather and Forecasting*, **20**, pp. 989–1005.

Bendix, J., Thies, B., Nauss, T. and Cermak, J., 2006, A feasibility study of daytime fog and low stratus detection with TERRA/AQUA-MODIS over land. *Meteorological Applications*, **13**, pp. 111–125.

Best, A.C., 1951, Drop-size distribution in cloud and fog. *Quarterly Journal of the Royal Meteorological Society*, **77**, pp. 418–426.

Betts, A.K., 1982, Cloud thermodynamic models in saturation point coordinates. *Journal of the Atmospheric Sciences*, **39**, pp. 2182–2191.

Betts, A.K. and Boers, R., 1990, A cloudiness transition in a marine boundary layer. *Journal of the Atmospheric Sciences*, **47**, pp. 1480–1497.

Boers, R. and Betts, A.K., 1988, Saturation point structure of marine stratocumulus clouds. *Journal of the Atmospheric Sciences*, **45**, pp. 1156–1175.

Boers, R., Melfi, S.H. and Palm, S.P., 1991, Cold-air outbreak during GALE: Lidar observations and modeling of boundary layer dynamics. *Monthly Weather Review*, **119**, pp. 1132–1150.

Boers, R. and Mitchell, R.M., 1994, Absorption feedback in stratocumulus clouds – influence on cloud top albedo. *Tellus*, **A46**, pp. 229–241.

Brenguier, J.L., Pawlowska, H. and Schüller, L., 2003, Cloud microphysical and radiative properties for parameterization and satellite monitoring of the indirect effect of aerosol on climate. *Journal of Geophysical Research*, **108**, pp. CMP 6-1–CMP 6-14.

Brenguier, J.L., Pawlowska, H., Schüller, L., Preusker, R. and Fischer, J., 2000, Radiative properties of boundary layer clouds: droplet effective radius versus number concentration. *Journal of the Atmospheric Sciences*, **57**, pp. 803–821.

Briggs, W.M. and Ruppert, D., 2004, Assessing the skill of yes/no forecasts for Markov observations. *Proceedings of 17th Conference on Probability and Statistics in the Atmospheric Sciences*, Seattle, Washington, (Boston, MA: American Metrological Society), pp. 1–20.

Brooks, H.E. and Doswell, C.A.I., 1996, A comparison of measures-oriented and distributions-oriented approaches to forecast verification. *Weather and Forecasting*, **11**, pp. 288–303.

Brown, R. and Roach, W.T., 1976, The physics of radiation fog: II – a numerical study. *Quarterly Journal of the Royal Meteorological Society*, **102**, pp. 335–354.

Caughey, S.J., Crease, B.A. and Roach, W.T., 1982, A field study of nocturnal stratocumulus: II – turbulence structure and entrainment. *Quarterly Journal of the Royal Meteorological Society*, **108**, pp. 125–144.

Cermak, J., 2006, SOFOS – a new satellite-based operational fog observation scheme. PhD thesis, Philipps-Universität Marburg.

Cermak, J. and Bendix, J., 2007, Dynamical nighttime fog/low stratus detection based on Meteosat SEVIRI data – a feasibility study. *Pure and Applied Geophysics*, **164**, pp. 1179–1192.

CERMAK, J. and BENDIX, J., 2008, A novel approach to fog/low stratus detection using Meteosat 8 data. *Atmospheric Research*, **87**, pp. 279–292.

CHANG, F.L. and LI, Z., 2002a, A bi-spectral near-infrared method for inferring the vertical variation of cloud droplet effective radius. *Proceedings of 11th Conference on Cloud Physics*, June 2002, Ogden, UT, pp. JP1.8.1–JP1.8.4 (Boston, MA: American Metrological Society).

CHANG, F.L. and LI, Z., 2002b, Estimating the vertical variation of cloud droplet effective radius using multispectral near-infrared satellite measurements. *Journal of Geophysical Research*, **107**, pp. AAC7-1–AAC7-12.

CHANG, F.L. and LI, Z., 2003, Retrieving vertical profiles of water-cloud droplet effective radius: algorithm modification and preliminary application. *Journal of Geophysical Research*, **108**, pp. AAC3-1–AAC3-11.

DOSWELL, C.A.I., DAVIES-JONES, R. and KELLER, D.L., 1990, On summary measures of skill in rare event forecasting based on contingency tables. *Weather and Forecasting*, **5**, pp. 576–585.

DRIEDONKS, A.G.M. and DUYNKERKE, P.G., 1989, Current problems in the stratocumulus-topped atmospheric boundary layer. *Boundary Layer Meteorology*, **46**, pp. 275–303.

DURAND, P. and BOURCY, T., 2001, Observations of the turbulence structure within two stratocumulus-topped marine boundary layers. *Boundary Layer Meteorology*, **99**, pp. 105–125.

ELLROD, G.P., 1995, Advances in the detection and analysis of fog at night using GOES multispectral infrared imagery. *Weather & Forecasting*, **10**, pp. 606–619.

ELLROD, G.P., 2002, Estimation of low cloud base heights at night from satellite infrared and surface temperature data. *National Weather Digest*, **26**, pp. 39–44.

EYRE, J.R., BROWNSCOMBE, J.L. and ALLAM, R.J., 1984, Detection of fog at night using Advanced Very High Resolution Radiometer (AVHRR) imagery. *Meteorological Magazine*, **113**, pp. 266–271.

FITZJARRALD, D.R. and LALA, G.G., 1989, Hudson Valley fog environments. *Journal of Applied Meteorology*, **28**, pp. 1303–1328.

GENIO, A.D.D. and WOLF, A.B., 2000, The temperature dependence of the liquid water path of low clouds in the southern Great Plains. *Journal of Climate*, **13**, pp. 3465–3486.

GERBER, H., 1981, Microstructure of a radiation fog. *Journal of the Atmospheric Sciences*, **38**, pp. 454–458.

GREENWALD, T.J. and CHRISTOPHER, S.A., 2000, The GOES I-M imagers: new tools for studying microphysical properties of boundary layer stratiform clouds. *Bulletin of the American Meteorological Society*, **81**, pp. 2607–2620.

GULTEPE, I. and ISAAC, G.A., 1997, Liquid water content and temperature relationship from aircraft observations and its applicability to GCMs. *Journal of Climate*, **10**, pp. 446–452.

GULTEPE, I., TARDIF, R., MICHAELIDES, S.C., CERMAK, J., BOTT, A., BENDIX, J., MÜLLER, M.D., PAGOWSKI, M., HANSEN, B., ELLROD, G., JACOBS, W., TOTH, G. and COBER, S.G., 2007, Fog research: a review of past achievements and future perspectives. *Pure and Applied Geophysics*, **164**, pp. 1121–1159.

HAYASAKA, T., NAKAJIMA, T., FUJIYOSHI, Y., ISHIZAKA, Y., TAKEDA, T. and TANAKA, M., 1995, Geometrical thickness, liquid water-content, and radiative properties of stratocumulus clouds over the western North Pacific. *Journal of Applied Meteorology*, **34**, pp. 460–470.

HEIDINGER, A.K. and STEPHENS, G.L., 2000, Molecular line absorption in a scattering atmosphere. Part II: application to remote sensing in the O2 A band. *Journal of the Atmospheric Sciences*, **57**, pp. 1615–1634.

HEINTZENBERG, J., WENDISCH, M., YUSKIEWICZ, B., ORSINI, D., WIEDENSOHLER, A., STRATMANN, F., FRANK, G., MARTINSSON, B.G., SCHELL, D., FUZZI, S. and ORSI, G., 1998, Characteristics of haze, mist and fog. *Beiträge zur Physik der Atmosphäre*, **71**, pp. 21–31.

Hess, M., Koepke, P. and Schult, U., 1998, Optical properties of aerosols and clouds: the software package OPAC. *Bulletin of the American Meteorological Society*, **79**, pp. 831–844.

Hoffmann, H.E. and Roth, R., 1989, Cloud physical parameters in dependence on height above cloud base in different clouds. *Meteorological and Atmospheric Physics*, **41**, pp. 247–254.

Hunt, G.E., 1973, Radiative properties of terrestrial clouds at visible and infra-red thermal window wavelengths. *Quarterly Journal of the Royal Meteorological Society*, **99**, pp. 346–369.

Hutchison, K.D., 2002, The retrieval of cloud base heights from MODIS and three-dimensional cloud fields from NASA's EOS Aqua mission. *International Journal of Remote Sensing*, **23**, pp. 5249–5265.

Iwabuchi, H. and Hayasaka, T., 2003, A multi-spectral non-local method for retrieval of boundary layer cloud properties from optical remote sensing data. *Remote Sensing of Environment*, **88**, pp. 249–308.

Jacobs, W., Nietosvaara, V., Bott, A., Bendix, J., Cermak, J., Michaelides, S. and Gultepe, I. (Eds.), 2008, *Short Range Forecasting Methods of Fog, Visibility and Low Clouds*, COST Action 722 final report (Brussels, Belgium: Office for Official Publications of the European Communities).

Kawamoto, K., Nakajima, T. and Nakajima, T.Y., 2001, A global determination of cloud microphysics with AVHRR remote sensing. *Journal of Climate*, **14**, pp. 2054–2068.

Korolev, A.V., Isaac, G.A., Mazin, I.P. and Barker, H.W., 2001, Microphysical properties of continental clouds from in-situ measurements. *Quarterly Journal of the Royal Meteorological Society*, **127**, pp. 2117–2151.

Liou, K.N., 2002, *An Introduction to Atmospheric Radiation*, International Geophysics Series, vol. 84 (London and San Diego, CA: Academic Press).

McFarlane, N.A., Boer, G.J., Blanchet, J.P. and Lazare, M., 1995, The Canadian Climate Centre second-generation general circulation model and its equilibrium climate. *Journal of Climate*, **5**, pp. 1013–1044.

Manton, M.J., 1983, The physics of clouds in the atmosphere. *Reports on Progress in Physics*, **46**, pp. 1393–1444.

Martin, G., Johnson, D. and Spice, A., 1994, The measurement and parameterization of effective radius and droplet in warm stratocumulus clouds. *Journal of the Atmospheric Sciences*, **51**, pp. 1823–1842.

Marzban, C., 1998, Scalar measures of performance in rare-event situations. *Weather and Forecasting*, **13**, pp. 753–763.

Marzban, C., 2004, The ROC curve and the area under it as performance measures. *Weather and Forecasting*, **19**, pp. 1106–1114.

Meyer, W.D. and Rao, G.V., 1999, Radiation fog prediction using a simple numerical model. *Pure and Applied Geophysics*, **155**, pp. 57–80.

Miles, N.L., Verlinde, J. and Clothiaux, E.E., 2000, Cloud droplet size distributions in low-level stratiform clouds. *Journal of the Atmospheric Sciences*, **57**, pp. 295–311.

Minnis, P., Heck, P.W., Young, D.F., Fairall, C.W. and Snider, J.B., 1992, Stratocumulus cloud properties derived from simultaneous satellite and island-based instrumentation during FIRE. *Journal of Applied Meteorology*, **31**, pp. 317–339.

Murphy, A.H., 1993, What is a good forecast? An essay on the nature of goodness in weather forecasting. *Weather and Forecasting*, **8**, pp. 281–293.

Nakajima, T.Y. and Nakajima, T., 1995, Wide-area determination of cloud microphysical properties from NOAA AVHRR measurements for FIRE and ASTEX regions. *Journal of the Atmospheric Sciences*, **52**, pp. 4043–4059.

Nauss, T., Kokhanovsky, A.A., Nakajima, T.Y., Reudenbach, C. and Bendix, J., 2005, The intercomparison of selected cloud retrieval algorithms. *Atmospheric Research*, **78**, pp. 46–78.

OLIVER, D.A., LEWELLEN, W.S. and WILLIAMSON, G.G., 1978, The interaction between turbulent and radiative transport in the development of fog and low-level stratus. *Journal of the Atmospheric Sciences*, **35**, pp. 301–316.

PINNICK, R.G., HOIHJELLE, D.L., FERNANDEZ, G., STENMARK, E.B., LINDBERG, J.D., HOIDALE, G.B. and JENNINGS, S.G., 1978, Vertical structure in atmospheric fog and haze and its effects on visible and infrared extinction. *Journal of the Atmospheric Sciences*, **35**, pp. 2020–2032.

PLATNICK, S., 2000, Vertical photon transport in cloud remote sensing problems. *Journal of Geophysical Research*, **105**, pp. 22919–22935.

PRUPPACHER, H.R. and KLETT, J.D., 1997, *Microphysics of Clouds and Precipitation*, 2, Atmospheric and Oceanographic Sciences Library, vol. 18 (Dordrecht, Boston, London: Kluwer).

ROACH, W.T., 1995, Back to basics: fog: part 2 – the formation and dissipation of land fog. *Weather*, **50**, pp. 7–11.

ROACH, W.T., BROWN, R., CAUGHEY, S.J., CREASE, B.A. and SLINGO, A., 1982, A field study of nocturnal stratocumulus: I – mean structure and budgets. *Quarterly Journal of the Royal Meteorological Society*, **108**, pp. 103–123.

SCHÜLLER, L., BENNARTZ, R., FISCHER, J. and BRENGUIER, J.L., 2005, An algorithm for the retrieval of droplet number concentration and geometrical thickness of stratiform marine boundary layer clouds applied to MODIS radiometric observations. *Journal of Applied Meteorology*, **44**, pp. 28–38.

SLINGO, A., BROWN, R. and WRENCH, C.L., 1982, A field study of nocturnal stratocumulus: III – high resolution radiative and microphysical observations. *Quarterly Journal of the Royal Meteorological Society*, **108**, pp. 145–165.

SLINGO, A. and SCHRECKER, H.M., 1982, On the shortwave radiative properties of stratiform water clouds. *Quarterly Journal of the Royal Meteorological Society*, **108**, pp. 407–426.

SOBRINO, J.A. and ROMAGUERA, M., 2004, Land surface temperature retrieval from MSG1-SEVIRI data. *Remote Sensing of Environment*, **92**, pp. 247–254.

STEPHENS, G.L., 1979, *Optical Properties of Eight Water Cloud Types*. Commonwealth Scientific and Industrial Research Organisation (CSIRO) Division of Atmospheric Physics technical Report 35, CSIRO.

STEPHENS, G.L., VANE, D.G., BOAIN, R.J., MACE, G.G., SASSEN, K., WANG, Z., ILLINGWORTH, A.J., O'CONNOR, E.J., ROSSOW, W.B., DURDEN, S.L., MILLER, S.D., AUSTIN, R.T., BENEDETTI, A., MITRESCU, C. and The CloudSat Science Team, 2002, The Cloudsat mission and the A-train – a new dimension of space-based observations of clouds and precipitation. *Bulletin of the American Meteorological Society*, **83**, pp. 1771–1790.

STEPHENSON, D.B., 2000, Use of the 'odds ratio' for diagnosing forecast skill. *Weather and Forecasting*, **15**, pp. 221–232.

THORNES, J.E. and STEPHENSON, D.B., 2001, How to judge the quality and value of weather forecast products. *Meteorological Applications*, **8**, pp. 307–314.

WALKER, M., 2003, The science of weather: radiation fog and steam fog. *Weather*, **58**, pp. 196–197.

WIEPRECHT, W., ACKER, K., MERTES, S., COLLETT, J., JAESCHKE, W., BRUGGEMANN, E., MOLLER, D. and HERRMANN, H., 2005, Cloud physics and cloud water sampler comparison during FEBUKO. *Atmospheric Environment*, **39**, pp. 4267–4277.

WILSON, L.J. and BURROWS, W.R., 2004, Spatial verification using the relative operating characteristic curve. In *Proceedings of 17th Conference on Probability and Statistics in the Atmospheric Sciences*, Seattle, Washington, (Boston, MA: American Metrological Society), pp. 2.8.1–2.8.6.

WRIGHT, B.J. and THOMAS, N., 1998, An objective visibility analysis and very-short-range forecasting system. *Meteorological Applications*, **5**, pp. 157–181.

ZHANG, H. and CASEY, T., 2000, Verification of categorical probability forecasts. *Weather and Forecasting*, **15**, pp. 80–89.